AGU PUBLICATIONS

JGR

Journal of Geophysical Research: Planets

RESEARCH ARTICLE
10.1002/2017JE005313

Key Points:
- ARTEMIS regularly observes protons reflected from lunar crustal magnetic fields
- Reflected protons traced from ARTEMIS to lunar surface to compile the global reflection map and scattering function
- Scattering function consistent with electrostatic fields as reflection mechanism from anomalies

Supporting Information:
- Supporting Information S1
- Data Set S1

Correspondence to:
A. R. Poppe,
poppe@ssl.berkeley.edu

Citation:
Poppe, A. R., J. S. Halekas, C. Lue, and S. Fatemi (2017), ARTEMIS observations of the solar wind proton scattering function from lunar crustal magnetic anomalies, *J. Geophys. Res. Planets*, *122*, doi:10.1002/2017JE005313.

Received 22 MAR 2017
Accepted 5 APR 2017
Accepted article online 10 APR 2017

ARTEMIS observations of the solar wind proton scattering function from lunar crustal magnetic anomalies

A. R. Poppe[1,2], J. S. Halekas[2,3], C. Lue[3], and S. Fatemi[1,2]

[1]Space Sciences Laboratory, University of California, Berkeley, California, USA, [2]Solar System Exploration Research Virtual Institute, NASA Ames Research Center, Moffett Field, California, USA, [3]Department of Physics and Astronomy, University of Iowa, Iowa City, Iowa, USA

Abstract Despite their small scales, lunar crustal magnetic fields are routinely associated with observations of reflected and/or backstreaming populations of solar wind protons. Solar wind proton reflection locally reduces the rate of space weathering of the lunar regolith, depresses local sputtering rates of neutrals into the lunar exosphere, and can trigger electromagnetic waves and small-scale collisionless shocks in the near-lunar space plasma environment. Thus, knowledge of both the magnitude and scattering function of solar wind protons from magnetic anomalies is crucial in understanding a wide variety of planetary phenomena at the Moon. We have compiled 5.5 years of ARTEMIS (Acceleration, Reconnection, Turbulence and Electrodynamics of the Moon's Interaction with the Sun) observations of reflected protons at the Moon and used a Liouville tracing method to ascertain each proton's reflection location and scattering angles. We find that solar wind proton reflection is largely correlated with crustal magnetic field strength, with anomalies such as South Pole/Aitken Basin (SPA), Mare Marginis, and Gerasimovich reflecting on average 5–12% of the solar wind flux while the unmagnetized surface reflects between 0.1 and 1% in charged form. We present the scattering function of solar wind protons off of the SPA anomaly, showing that the scattering transitions from isotropic at low solar zenith angles to strongly forward scattering at solar zenith angles near 90°. Such scattering is consistent with simulations that have suggested electrostatic fields as the primary mechanism for solar wind proton reflection from crustal magnetic anomalies.

1. Introduction

While the Moon is to first order a simple plasma absorbing object with no global upstream bow shock, lunar crustal magnetic fields can significantly perturb this picture up to regional scales. Lunar crustal magnetic fields are heterogeneously dispersed across the lunar surface on scales ranging from one to thousands of kilometers with strengths up to at least hundreds of nanoTesla [*Hood et al.*, 1981; *Halekas et al.*, 2001; *Mitchell et al.*, 2008; *Purucker and Nicholas*, 2010]. Previous in situ measurements by spacecraft have observed a wealth of plasma phenomena associated with lunar crustal magnetic anomalies, including reflected proton populations [*Futaana et al.*, 2003; *Saito et al.*, 2010; *Lue et al.*, 2011; *Halekas et al.*, 2013], ambipolar electrostatic fields [*Saito et al.*, 2012], limb compressions and/or shocks [*Russell and Lichtenstein*, 1975; *Halekas et al.*, 2006a, 2014], and a variety of electromagnetic waves [e.g., *Halekas et al.*, 2006b, 2008; *Tsugawa et al.*, 2011; *Harada et al.*, 2015]. Energetic neutral atom (ENA) observations have also provided evidence that lunar magnetic anomalies can deflect and/or reflect solar wind protons before they strike the surface via the development of large-scale electrostatic potentials [*Wieser et al.*, 2010; *Vorburger et al.*, 2012; *Futaana et al.*, 2013].

Numerous investigations have explored the potential mechanisms at work within crustal magnetic anomalies with laboratory experiments [*Wang et al.*, 2012, 2013] and numerical simulations, including magnetohydrodynamic (MHD) [e.g., *Harnett and Winglee*, 2002, 2003; *Xie et al.*, 2015], hybrid [*Fatemi et al.*, 2014, 2015; *Jarvinen et al.*, 2014; *Giacalone and Hood*, 2015; *Poppe et al.*, 2016], and kinetic/particle-in-cell methodologies [e.g., *Poppe et al.*, 2012; *Deca et al.*, 2014, 2015; *Zimmerman et al.*, 2015; *Bamford et al.*, 2016]. These simulations have suggested that large-scale ambipolar and/or Hall electrostatic fields may be the primary mechanism of proton reflection from lunar crustal magnetic fields, rather than magnetic reflection. Indeed, Kaguya observations of simultaneously decelerated solar wind protons and accelerated solar wind electrons over a magnetic anomaly have been interpreted as electrostatic fields [*Saito et al.*, 2012]; however, direct measurements of this have proven rare. Reflected protons are much more often seen in correlation with crustal anomalies and thus present a powerful data set with which to constrain various models of solar wind/crustal field interactions.

Shielding of the lunar surface by crustal magnetic anomalies has implications for weathering of the lunar regolith, the formation and variability of the lunar neutral exosphere, and the lunar plasma environment. Protons that are reflected by crustal magnetic anomalies before striking the lunar surface do not participate in space weathering of lunar regolith, a process that changes the chemical and optical characteristics of regolith grains [e.g., *Richmond et al.*, 2003; *Loeffler et al.*, 2009; *Kramer et al.*, 2011; *Hemingway et al.*, 2015]. The reduction of local space weathering rates due to crustal magnetic anomalies is one of the leading theories for the formation of lunar swirls, which are sinuous, superficial, high-albedo markings on the lunar surface [e.g., *Hood and Schubert*, 1980; *Hood and Williams*, 1989]. Crustal magnetic anomalies are also believed to play a role in locally suppressing the formation of the lunar neutral exosphere by decelerating and/or reflecting solar wind protons such that charged-particle sputtering of the lunar surface is locally diminished [*Poppe et al.*, 2014]. Preliminary evidence for this phenomenon has been identified in ARTEMIS (Acceleration, Reconnection, Turbulence and Electrodynamics of the Moon's Interaction with the Sun) observations of exospheric pickup ion distributions at the Moon [*Halekas et al.*, 2016]. Finally, the reflection of solar wind protons from crustal anomalies has significant impact on the near-lunar plasma environment. Reflected protons generate both limb compressions and shocks [e.g., *Russell et al.*, 1973; *Fatemi et al.*, 2014; *Halekas et al.*, 2014] and disturbances in the lunar wake [*Nishino et al.*, 2009; *Dhanya et al.*, 2016] as reflected protons are "repicked up" in the solar wind flow. Thus, understanding each of these separate phenomena requires an accurate and detailed understanding of the magnitude and variability of solar wind proton reflection from lunar crustal magnetic fields.

Here we present an analysis of more than 5 years of ARTEMIS observations of reflected solar wind protons from lunar crustal magnetic anomalies. We use a backward Liouville tracing method to map ARTEMIS observations at altitude to reflection locations and angles at the lunar surface. Section 2 describes an example ARTEMIS observation of reflected protons and the methodology for tracing the proton observations back to the lunar surface. Section 3 presents the global map of reflected solar wind protons from the lunar surface compiled from more than 5 years of ARTEMIS data, while section 4 presents the solar wind proton scattering function off of the South Pole/Aitken Basin magnetic anomaly. Finally, we discuss the results and conclude in sections 5 and 6, respectively.

2. ARTEMIS Observation: 2 July 2014

The ARTEMIS mission consists of two identical probes, termed P1 and P2, respectively, with low- and high-energy ion and electron spectrometers and electric and magnetic field measurements [*McFadden et al.*, 2008; *Auster et al.*, 2008; *Angelopoulos*, 2011]. Both probes are in highly elliptical, near-equatorial orbits around the Moon with periselenes between 10 and 1000 km and aposelenes of ≈20,000 km (≈10 lunar radii) and have been nominally operating in lunar orbit since mid-2011. During many of the ARTEMIS periselene passages, ion fluxes at energies and angles other than the solar wind are routinely observed. Figure 1 shows an ARTEMIS observation of reflected solar wind protons on 2 July 2014, including (a) the lunar position with respect to the Earth in Geocentric-Solar-Ecliptic (GSE) coordinates, (b) the ARTEMIS P1 and P2 positions with respect to the Moon in Selenocentric-Solar-Ecliptic (SSE) coordinates, (c) P1 ion energy flux, (d) P2 ion energy flux, (e) P1 magnetic field, (f) P1 electric field, (g) P1 and P2 altitudes, respectively, and (h) the P1 solar zenith angle. P1 flies through a periselene of ≈450 km near 20° solar zenith angle while P2 remains above 2000 km and off the dawn flank of the Moon. By comparing the ARTEMIS ion energy spectra in Figures 1c and 1d, one sees that ARTEMIS P1 observes the solar wind proton beam at energies near 430 eV (≈280 km/s) and an additional population of protons at energies from 100 eV to 2 keV not seen by ARTEMIS P2.

To further explore this additional population of protons, we computed energy distributions for both probes for two separate populations: (i) those protons with velocities within a cone angle of 30° of the direction of the solar wind (-X SSE) and (ii) those protons with velocities outside this cone (i.e., nonsolar wind). Figure 2 compares these two energy distributions for both probes. Figures 2a and 2b show the solar wind-only ions for P1 and P2, respectively, while Figures 2c and 2d show the nonsolar wind ions for each probe. One can clearly see that P1 observes the additional population of nonsolar wind protons while P2 observes only the solar wind. Given that P1 flies through a periselene of ≈450 km while P2 is greater than 2000 km from the Moon during this time, we can safely conclude that P1 is observing protons that have interacted with and been reflected from the Moon. Figures 2e and 2f show the angular ion spectra for P1 and P2 during this time,

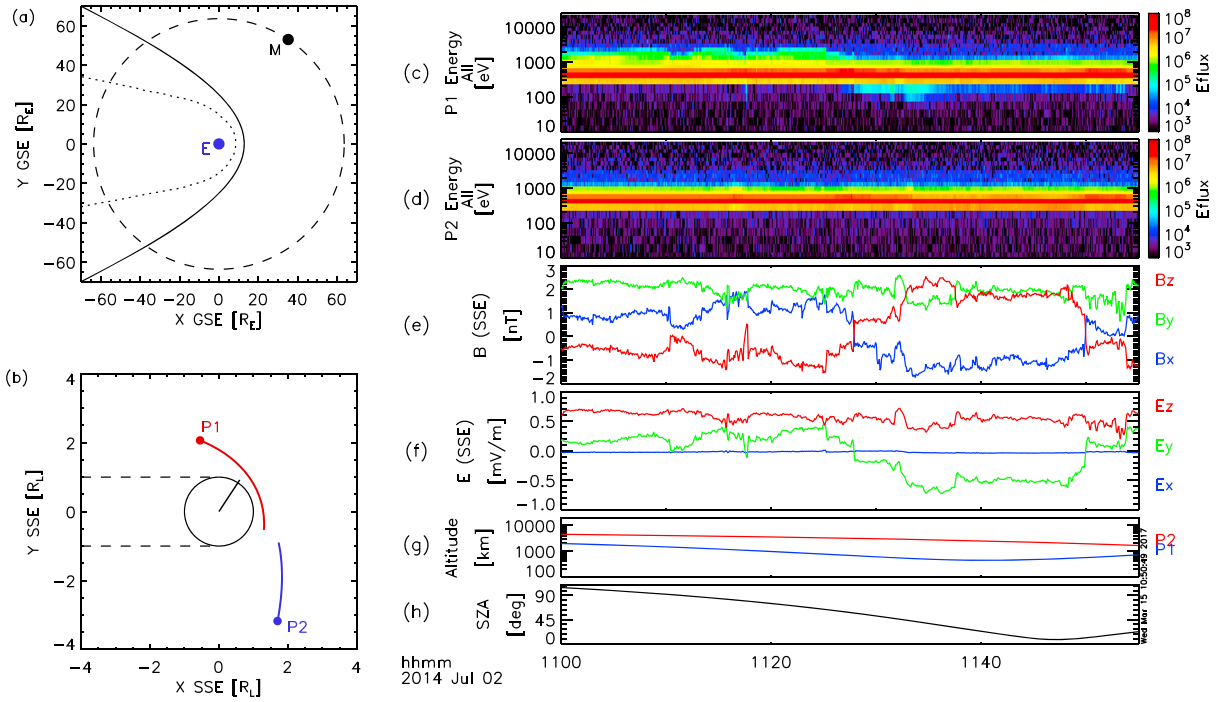

Figure 1. (a–h) ARTEMIS observations of solar wind protons reflected from the South Pole-Aitken Basin anomaly on 2 July 2014 as described in the text.

with the main solar wind beam observed by both probes at approximately 180° (i.e., in the antisolar direction) with the additional population of protons seen varying across all other (i.e., nonsolar wind) angles in P1 only. Finally, we computed the partial density as seen by P1 for the solar wind population and nonsolar wind (or "reflected") population, shown in Figure 2f. The reflected population is approximately 20% of the solar wind density through the entire observation.

To identify the reflection location for the nonsolar wind protons observed by P1, we used a backward Liouville tracing algorithm making use of the conservation of particle phase space density along trajectories [e.g., *Fatemi et al.*, 2012]. We used ARTEMIS Electrostatic Analyzer (ESA) *reduced* ion data which measures the ion distribution function in 24 logarithmic energy bins from 1 to 25,000 eV and 50 angular bins covering 4π str every spin period (≈4.3 s) [see *McFadden et al.*, 2008]. Each ARTEMIS observation was first converted to phase space density and stored in a distribution function, $f(\mathbf{r}, \mathbf{v})$ (in units of $s^3\ m^{-6}$), as a function of observed time, angle, and energy (velocity). With the electric and magnetic fields measured locally by ARTEMIS, a fourth-order Runge-Kutta integration was used to trace the trajectory of each nonsolar wind observation backward in time from the ARTEMIS position until the trajectory either struck the Moon or left a 2 R_L (lunar radii) sphere centered on the Moon. Given typical proton gyroradii in the solar wind of ~0.5 R_L, this is a sufficient volume to accurately capture the reflected proton dynamics. We note that this tracing method does not include electric and magnetic fields from the crustal magnetic anomalies themselves and thus is subject to some error close to the lunar surface (<≈30 km altitude). This error will contribute some amount of blurring of the reflected proton locations; however, we expect this to be small relative to our chosen spatial distribution mapped onto the lunar surface.

For trajectories that struck the Moon, we recorded the reflection location (including both solar zenith angle and selenographic longitude/latitude), scattered velocity and angle, phase space density, upstream solar wind parameters, and interplanetary magnetic field (IMF) orientation. After all individual traces from the flyby were completed, we constructed phase space distributions, $f_{sc}^{(\phi,\theta)}(\mathbf{v})$, for the scattered distribution at each spatial point on the lunar surface (denoted by longitude, ϕ, and latitude, θ) with 5° × 5° spatial resolution. Using the subset of trajectories that traced back to each spatial bin on the lunar surface, we populated the local scattered distribution function with the average of all trajectories that fell within each 3-D velocity bin. At each location,

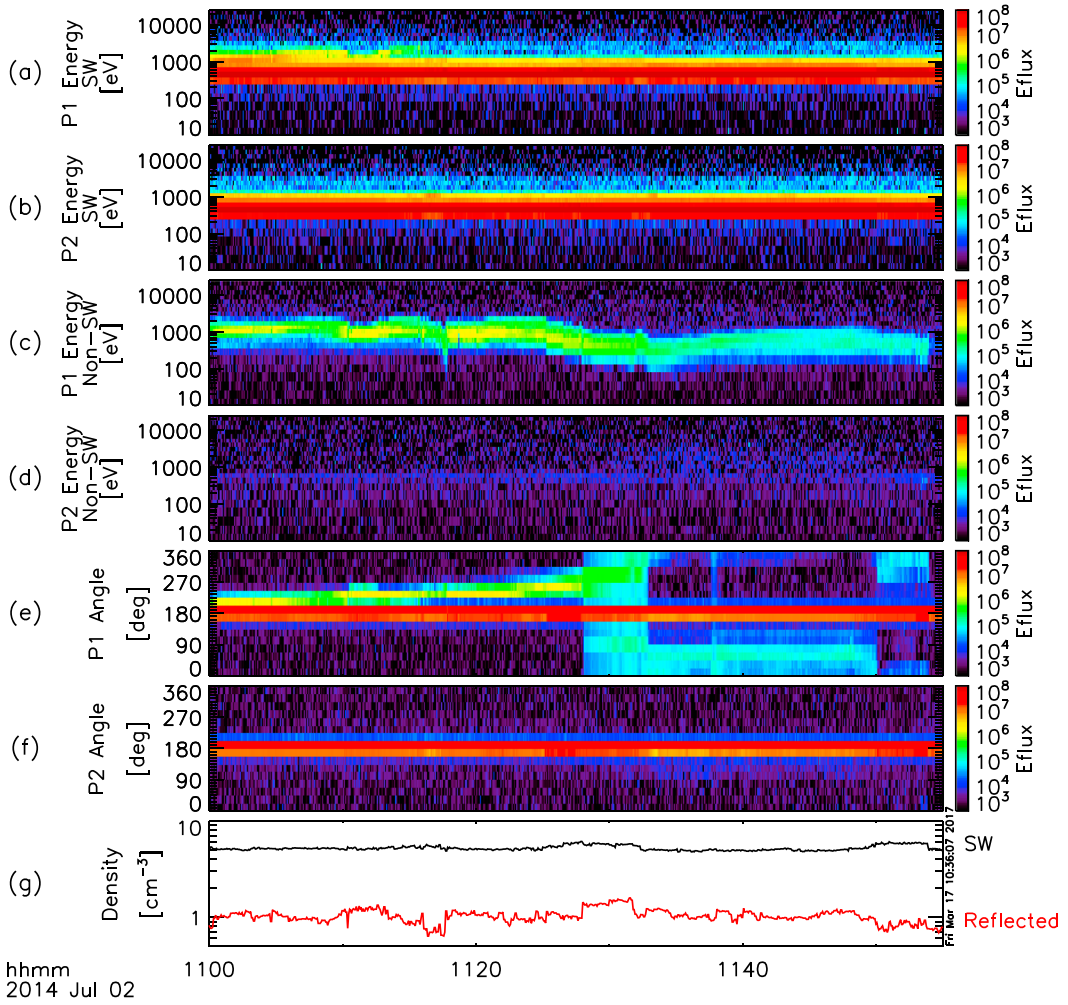

Figure 2. (a–g) A comparison of solar wind and nonsolar wind populations from both ARTEMIS probes on 2 July 2014.

$f_{sc}^{(\phi,\theta)}(\mathbf{v})$ can then be used to determine the moments of the scattered proton distribution, for example, the scattered flux, $\mathbf{\Gamma}_{sc}(\phi,\theta)$, as a function of selenographic location $[\phi,\theta]$, given by,

$$\mathbf{\Gamma}_{sc}(\phi,\theta) = \int d\mathbf{v}\, \mathbf{v} f_{sc}^{(\phi,\theta)}(\mathbf{v}), \tag{1}$$

where we have integrated over the scattered proton velocity vector, **v**.

Figure 3 shows the results of the backward Liouville tracing algorithm for the single P1 lunar flyby shown in Figure 1, including (a) the lunar surface crustal magnetic field strength [*Purucker and Nicholas*, 2010], and the 5° × 5° spatial distribution of (b) the total number of particle trajectories backtraced from ARTEMIS P1 to the lunar surface and (c) the reflected proton flux relative to the incident solar wind flux. Figure 3b shows that for the 2 July 2014 flyby, particle trajectories traced back from ARTEMIS P1 to a broad swath of the moon spanning longitudes between 50° and 180° and latitudes between −70° and 40° with the highest concentration of locations centered under the ARTEMIS periselene location near selenographic latitude/longitude of [−10°, 140°]. This region includes several groups of crustal magnetic fields including the South Pole-Aitken Basin, Firsov, and Mare Moscoviense anomalies. The reflected proton flux (i.e., the result of equation (1)) mapped back from this observation, Figure 3c, shows that the reflected protons observed by ARTEMIS P1 on 2 July 2014 originated mainly from the northwest corner of the highly magnetized South Pole-Aitken (SPA) Basin. The reflected flux observed by ARTEMIS P1 peaks at approximately 0.2% of the incoming solar wind flux. We stress that the reflection percentage observed on this single ARTEMIS flyby represents only a small fraction of the total reflected solar wind flux from any given location on the lunar surface. For each ARTEMIS flyby, only a fraction of all scattered velocity vectors from a given location on the surface can intersect the spacecraft

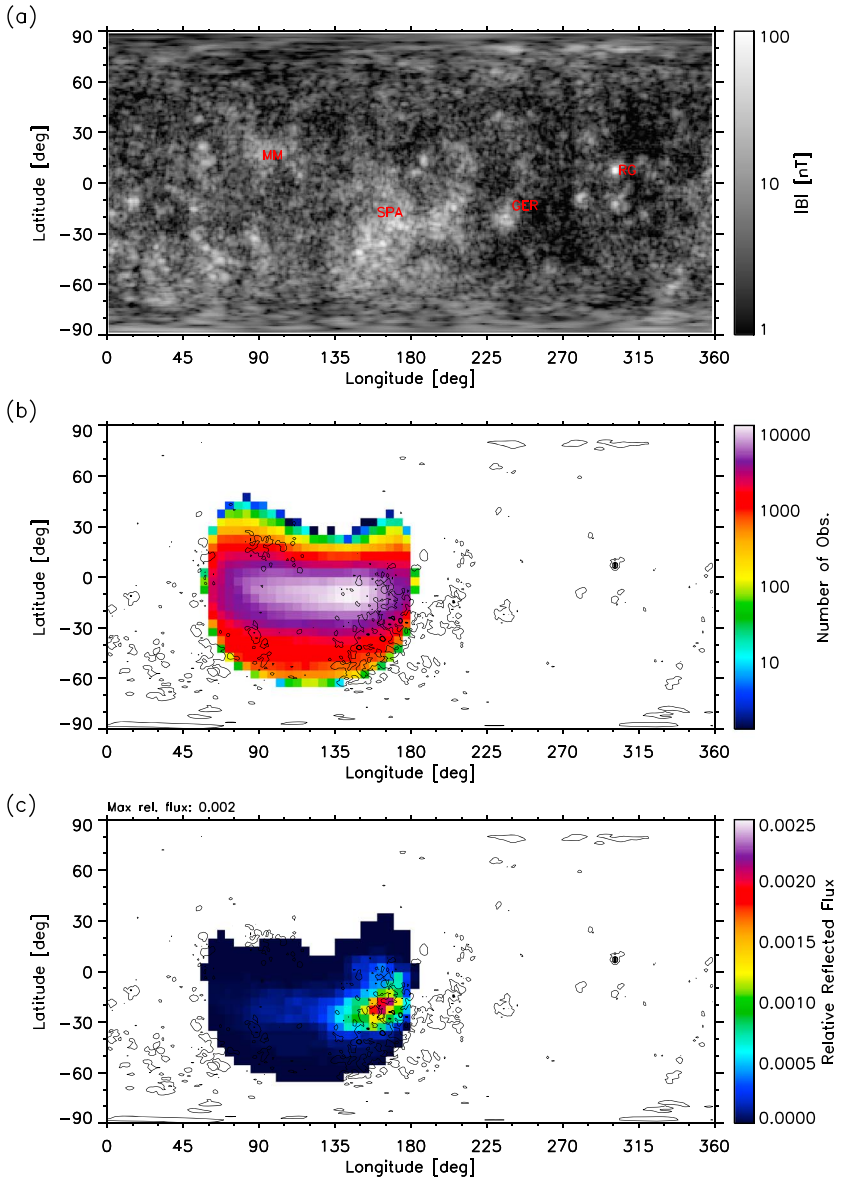

Figure 3. Backtracing results for ARTEMIS P1 observations on 2 July 2014 (Figure 1): (a) The surface crustal magnetic field strength [*Purucker and Nicholas*, 2010], (b) the number of observations traced back to each 5 × 5° latitude and longitude bin, and (c) the reflected proton flux relative to the incident solar wind flux. Red labels in Figure 3a denote prominent magnetic anomalies: Mare Marginis (MM), South Pole/Aitken Basin (SPA), Gerasimovich (GER), and Reiner Gamma (RG). In Figures 3b and 3c, contours denote the modeled lunar surface crustal magnetic field strengths of 10, 50, and 100 nT [*Purucker and Nicholas*, 2010].

orbital trajectory, and thus, the total reflection percentage at each location must be obtained from aggregating observations from many ARTEMIS flybys (see section 3). Nevertheless, the observations from ARTEMIS P1 on 2 July 2014 are consistent with previous observations that indicate significant reflection of solar wind protons from crustal magnetic anomalies such as SPA [e.g., *Lue et al.*, 2011].

3. Global Proton Reflection Map

Using the methodology outlined in section 2, we processed all currently available ARTEMIS observations (September 2011 to January 2017, nearly the entirety of the ARTEMIS mission to date) in order to construct a global map of proton reflection efficiency. We selected only observations that satisfied several conditions: (1) the Moon was located in the solar wind (i.e., outside of the terrestrial magnetosheath or magnetotail),

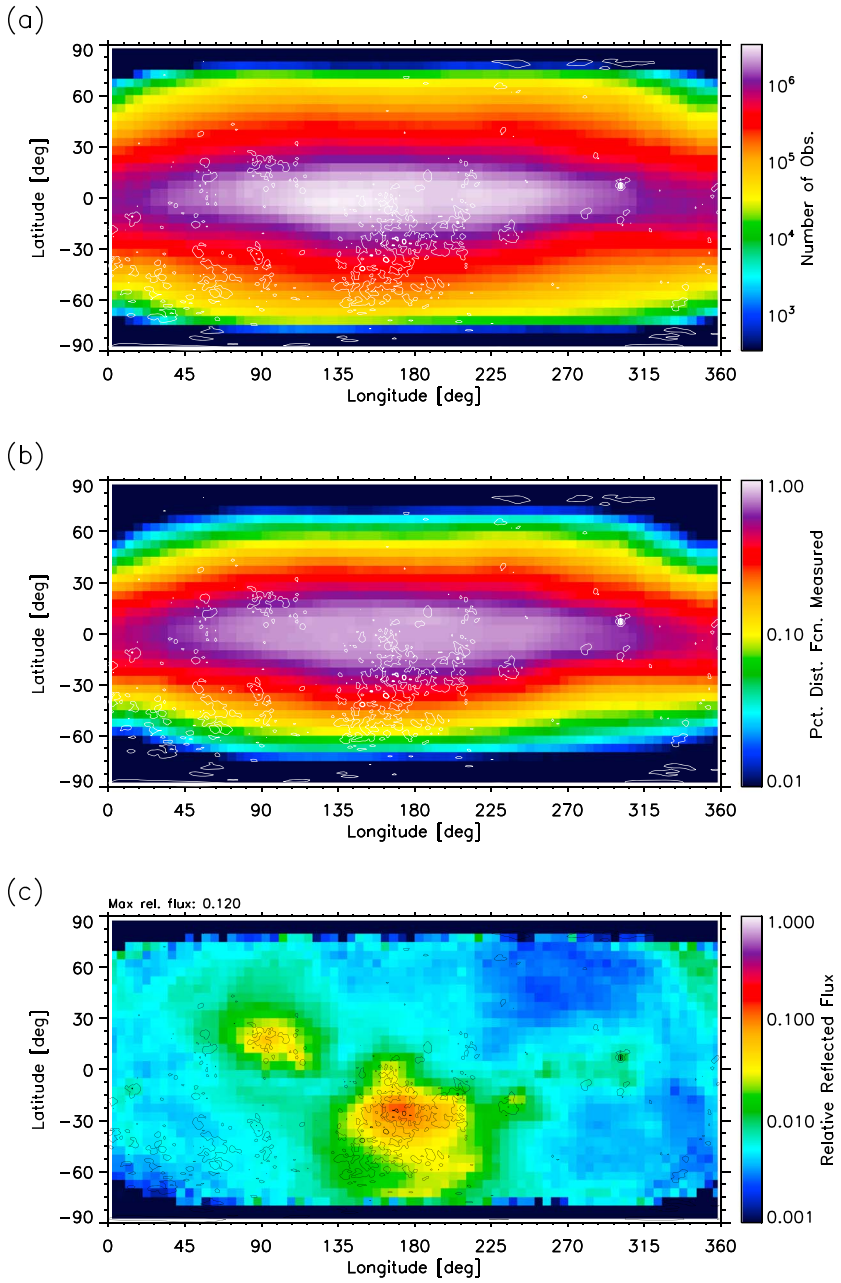

Figure 4. Backtracing results for 1602 compiled ARTEMIS observations: (a) The total number of observations per spatial bin, (b) the percentage of the reflected proton velocity distribution, $f_{sc}^{(\phi,\theta)}(\mathbf{v})$, in each spatial bin, and (c) the average reflected solar wind proton flux. Data for Figure 4c are provided in the supporting information.

(2) no terrestrial foreshock ions were present in the ESA data, and (3) the ARTEMIS trajectory crossed through a hemispherical volume of space 2 R_L in radius on the dayside of the Moon. The first two filters ensure that any observed nonsolar wind species are indeed due to reflection from the lunar surface or crustal magnetic fields. The third filter selects all regions where ARTEMIS will observe reflected protons given that typical gyroradii of reflected protons range between 0.2 and 1.5 R_L (350–2500 km, assuming typical ranges of solar wind velocities, [275, 600] km/s, and interplanetary magnetic field strengths, [2.5, 7.5] nT). We note that the orbital design of the ARTEMIS mission is favorable for mapping of reflected proton distributions since the ARTEMIS periselenes occur over all lunar local times (or equivalently, solar zenith angle) and lunar selenographic location (i.e., nearside/farside) [*Sweetser et al.*, 2011], although one limitation is the generally ecliptic orbits of ARTEMIS which does partially limit the ability to observe reflection from high latitudes. We also filtered the

ARTEMIS data by upstream solar wind conditions, selecting only data with solar wind density, $1 < n_{sw} < 10\,cm^{-3}$ and solar wind velocity, $275 < v_{sw} < 600$ km/s. This was implemented to ensure that observations were chosen from "nominal" solar wind conditions [e.g., *Dmitriev et al.*, 2011], excluding, for example, coronal mass ejections, major interplanetary shocks, and other heliospheric disturbances. Following these filters, all ESA proton velocity vectors were then traced backward in time, and if the trajectory struck the Moon, all associated metadata were recorded. In total, we processed 1602 ARTEMIS flybys (811 for P1, 791 for P2) which yielded $>1.5 \times 10^9$ individual measurements of reflected proton distribution function from across the lunar surface.

To compute the reflection map for all locations across the lunar surface, we took three additional steps. First, each measured distribution function was normalized by the incoming solar wind flux. Second, we averaged all measured values of the reflected distribution function for instances in which ARTEMIS measured the reflected distribution function for a specific spatial location and scattered velocity multiple times. Third, for instances in which ARTEMIS made no measurements of the reflected distribution function at a specific location and scattered velocity, we filled such bins in the distribution function with the average measured distribution function at the same scattered speed and the same spatial location. The third step is critical in ensuring that we do not artificially underreport the reflected flux due to the fact that the ARTEMIS observations do not cover the entire reflected proton distribution at every point on the lunar surface.

Figure 4a shows the distribution of the 1.5×10^9 proton reflection points obtained from the backtracing algorithm for all ARTEMIS measurements displayed in selenographic coordinates (0° is the nearside, 180° the farside). The observations cluster strongly near the equatorial plane due to the low-inclination ARTEMIS orbits. The observations also peak on the farside and have a minimum on the nearside, as the lunar nearside is mainly within the terrestrial magnetotail during local daytimes (and thus, is often excluded from this analysis). Figure 4b shows the fraction of the reflected velocity distribution, $f_{sc}^{(\phi,\theta)}(\mathbf{v})$, measured by ARTEMIS within each 5° × 5° spatial bin on the surface, with greater than 80% measured in the equatorial region. Similar to Figure 4a, the measured fraction declines both toward the lunar nearside and toward higher latitudes. For latitudes greater than 60°, 10% or less of the distribution function has been measured by ARTEMIS and, thus, total reflected flux values above these latitudes carry greater uncertainty than those at lower latitudes.

Figure 4c shows the fraction of reflected proton flux relative to the incoming solar wind flux as a function of selenographic longitude and latitude. The highest levels of reflected flux are associated with several groupings of magnetic anomalies, including South Pole/Aitken Basin, Mare Marginis, and Gerasimovich. At the 5× 5° spatial resolution presented here, the maximum reflected flux is 12% of the incoming solar wind flux, consistent with Chandrayaan measurements [*Lue et al.*, 2011]. Most of the unmagnetized lunar surface reflects between 0.1% and 1% of the solar wind flux, also in line with previous observations [*Saito et al.*, 2008]. Not all magnetic anomalies display solar wind reflection above the 0.1 – 1% typical of the unmagnetized surface, including, for example, the various magnetic anomalies in the southern hemisphere at selenographic longitudes of 0 – 90°; however, this could be observational bias since ARTEMIS cannot observe protons strongly forward scattered from high latitudes. The Reiner Gamma magnetic anomaly displays a reflection fraction only slightly above 1%; however, this relatively low value is attributed to the small spatial size of Reiner Gamma (≈1.5° × 1.5°) with respect to the 5° × 5° spatial bins used here, such that the locally strong reflection from Reiner Gamma is averaged with neighboring unmagnetized surface at lower reflection values.

4. Magnetic Anomaly Scattering Function

In addition to calculating the net reflected solar wind flux from lunar crustal magnetic anomalies, the backward Liouville tracing algorithm also allows study of the scattering function of solar wind protons off of lunar magnetic anomalies. At any spatial point on the lunar surface, the reduced angular distribution function, $F(\psi, \chi)$, where ψ is the azimuthal angle and χ is the polar angle in a local coordinate system normal to the surface (i.e., χ is defined with respect to the local surface normal at each location and ψ is defined such that $\psi = 0°$ is toward the Sun and $\psi = 180°$ is antisunward), can be calculated as

$$F^{(\phi,\theta)}(\psi, \chi) = \int_0^\infty f_{sc}^{(\phi,\theta)}(v, \psi, \chi) v^2 dv, \quad (2)$$

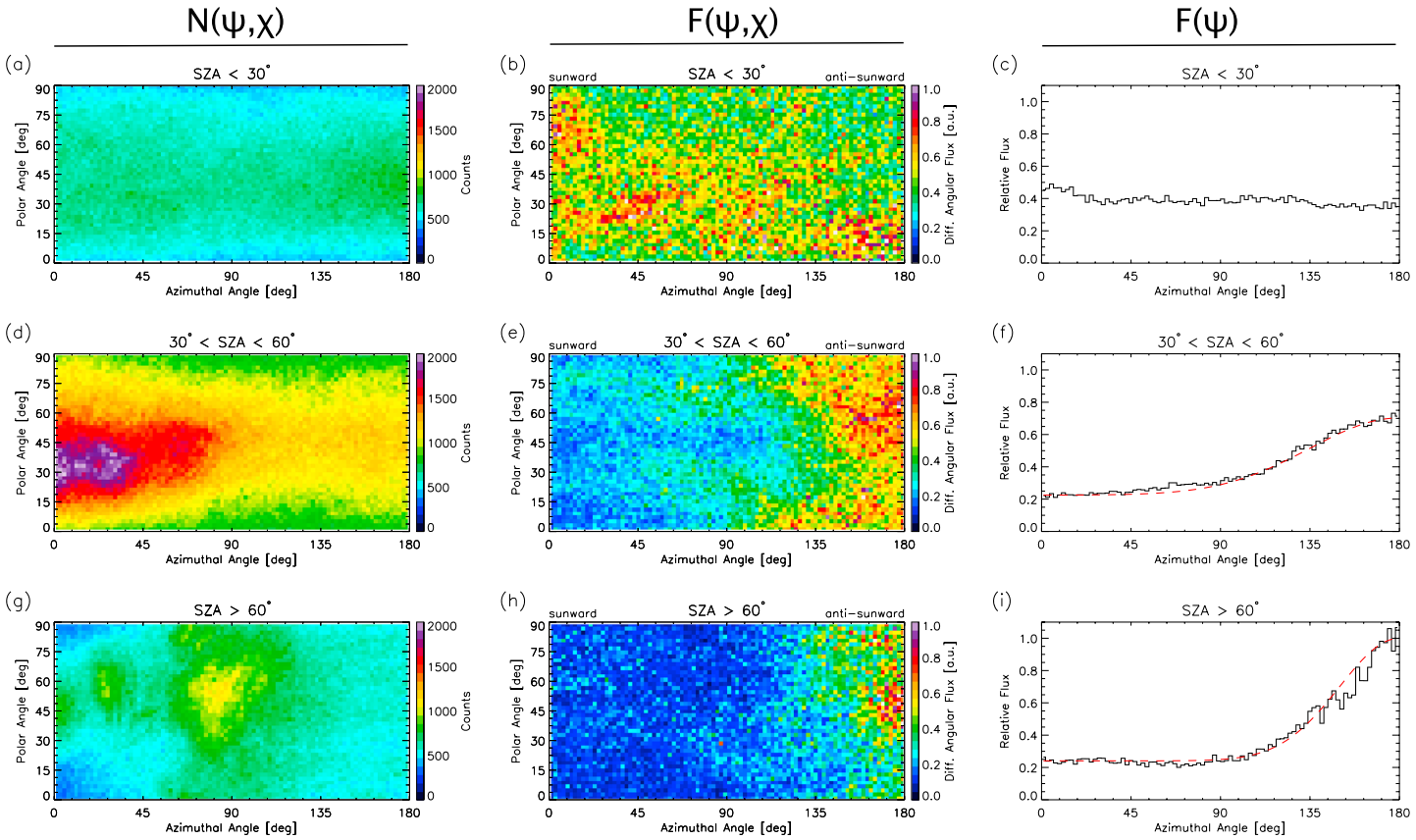

Figure 5. The angular scattering functions for the South/Pole/Aitken Basin magnetic anomaly for different cuts in solar zenith angle. (a, d, and g) The number of observations per bin. (b, e, and h) The two-dimensional scattering function; (c, f, and i) the reduced, one-dimensional angular scattering function as a function of the azimuthal angle. The red dashed line in Figures 5f and 5i show the empirical fit, as discussed in the text.

where $f_{sc}^{(\phi,\theta)}(v,\psi,\chi)$ is the full scattered distribution function at any spatial point and v is the reflected proton speed. The distribution function can be further reduced to also study scattering against the azimuthal angle only as

$$F^{(\phi,\theta)}(\psi) = \int_0^{\pi/2}\int_0^{\infty} f_{sc}^{(\phi,\theta)}(v,\psi,\chi)v^2\sin(\chi)\mathrm{d}v\mathrm{d}\chi, \quad (3)$$

by integrating over both the speed, v, and polar angle, χ.

Using the reflected distribution function compiled in section 3, we calculated both reduced angular distribution functions for the South Pole/Aitken Basin anomaly, for three separate ranges of solar zenith angle, α: (1) $\alpha < 30°$, (2) $30° < \alpha < 60°$, and (3) $60° < \alpha < 80°$. We excluded solar zenith angles greater than 80° from our analysis as we found that the occasional presence of limb shocks and/or compressions [e.g., *Russell and Lichtenstein*, 1975; *Halekas et al.*, 2014] contaminated the backtracing of proton trajectories due to highly disturbed magnetic and electric fields in the vicinity of the limb. Figure 5 shows the number of observations per angular bin, $N(\psi,\chi)$, and the two reduced distribution functions, $F(\psi,\chi)$ and $F(\psi)$, for each range of solar zenith angle, respectively. All three ranges in solar zenith angle possess sufficient statistics (i.e., at least several hundred observations per angular bin). In Figures 5b and 5c, the angular scattering function is broadly isotropic in both polar and azimuthal angles for $\alpha < 30°$. For $30° < \alpha < 60°$, shown in Figures 5e and 5f, the angular scattering function contains both an isotropic component and a forward scattering component [e.g., *Fatemi et al.*, 2014, Figure, 2]. In Figure 5f, we overplot as the red dashed curve an empirically fit function of a constant term plus a forward scattering Gaussian, $F(\psi) = 0.25 + 0.48\exp(-(180-\psi)^2/2\sigma^2)$, where $\sigma = 45°$. Finally, Figures 5h and 5i show the angular scattering function for $\alpha > 60°$, which displays both the isotropic component and a strongly forward scattering angular distribution. Figure 5h also shows stronger scattering toward $\chi = 90°$ (i.e., perpendicular to the local surface normal). The empirically fit azimuthal scattering curve for this case, shown in Figure 5i, is $F(\psi) = 0.25 + 0.75\exp(-(180-\psi)^2/2\sigma^2)$, where $\sigma = 30°$.

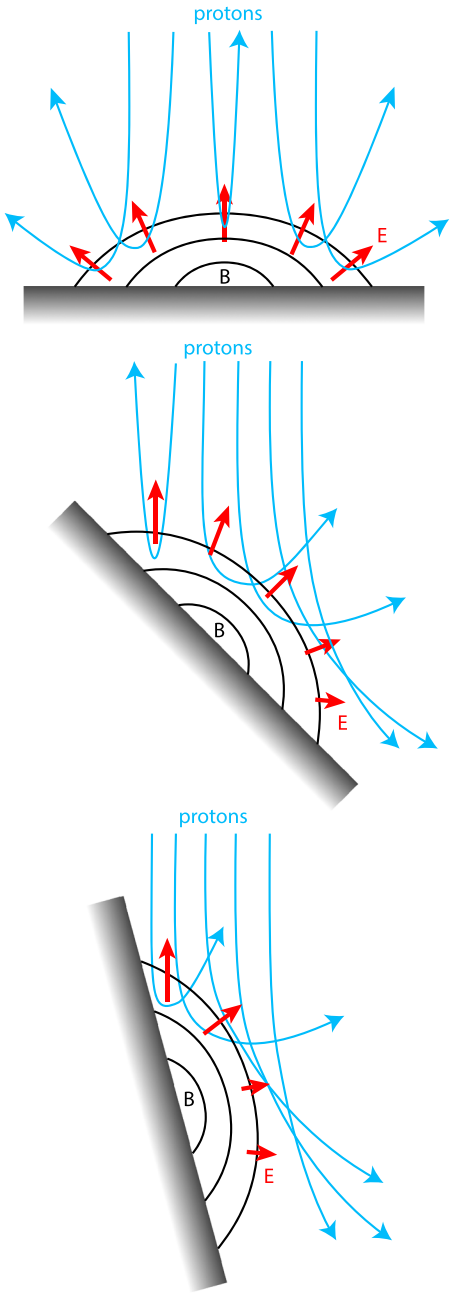

Figure 6. A cartoon of proton scattering from lunar magnetic anomalies for (top, middle, and bottom) different incident solar zenith angles.

5. Discussion

Similar to previous observations by both the Kaguya [*Saito et al.*, 2008, 2012] and Chandrayaan spacecraft [*Lue et al.*, 2011], ARTEMIS observes the highest percentage of reflected solar wind flux over regions of strong crustal magnetic anomalies. The two strongest regions of solar wind proton reflection are the South Pole/Aitken Basin on the lunar farside and Mare Marginis near 90° longitude, with maximum reflected flux fractions of 12% and 5.5%, respectively. The Gerasimovich anomaly near 230° longitude is also visible with a peak reflection fraction of 2.5% and the Reiner Gamma magnetic anomaly near 300° longitude registers 1.1% solar wind reflection. The unmagnetized lunar surface reflects between 0.1 and 1% of the solar wind in charged form. We again note that anomalies significantly smaller than our spatial resolution of $5° \times 5°$ will appear with a reduced reflected fraction, as any reflection is averaged out with nearby unmagnetized surface. Higher spatial resolution mapping may be possible with improved computational resources; however, the error inherent in the ARTEMIS observations (i.e., finite angle and energy bin widths), the Runge-Kutta backtracing, and the lack of exact knowledge of the electromagnetic fields within anomalies (especially very close to the surface) prevents higher-resolution mapping. Nevertheless, we note that the reflection map produced here agrees well with that from Chandrayaan [*Lue et al.*, 2011] and Kaguya [*Poppe et al.*, 2014].

The ARTEMIS observations, averaged over upstream conditions, show that reflection from the South Pole/Aitken Basin crustal magnetic anomaly is well described by two components: an isotropic function and a forward scattered Gaussian function with a strength and width that is dependent on the solar zenith angle of the anomaly. For low solar zenith angles, depicted as a cartoon in Figure 6 (top), simulations suggest that the electrostatic fields within the anomaly are roughly normal to a hemispherically shaped surface [e.g., *Jarvinen et al.*, 2014, Figure 3], and thus, the outgoing angle of a scattered solar wind proton would roughly depend on the impact parameter relative to the center of the anomaly. At low SZA, solar wind protons are incident on anomalies at a full range of impact parameters and thus, the electrostatic fields would scatter and reflect the protons nearly evenly over 2π [see, e.g., *Zimmerman et al.*, 2015, Figure 6b]. At moderate solar zenith angles, Figure 6 (middle), the isotropic scattering is still generally present yet protons that have larger impact parameters to the anomaly experience an electrostatic field more transverse to their undisturbed momentum vector and thus have a net scattered velocity vector both in the transverse and forward directions. This yields a broad forward scattering component to the distribution. Finally, for large solar zenith angles, Figure 6 (bottom), the majority of solar wind protons are incident to the anomaly at large impact angles

relative to the local surface normal and thus are more likely to receive only transverse momentum from the electrostatic fields within the anomaly. In turn, this leads to a relatively small isotropic component and a larger forward scattering component.

This scattering function is consistent with the proposed theory that proton reflection from crustal magnetic anomalies is mainly due to the presence of large electrostatic fields above and within the anomaly [e.g., *Wang et al.*, 2012, 2013; *Jarvinen et al.*, 2014; *Fatemi*, 2014; *Fatemi et al.*, 2015; *Deca et al.*, 2015; *Zimmerman et al.*, 2015]. Specifically, *Zimmerman et al.* [2015] used an electrostatic particle-in-cell model to study the possible mechanism(s) of proton reflection from crustal magnetic fields. By comparing simulation runs with both electric and magnetic fields and simulations with only magnetic fields, they found that the magnetic fields were unable to deflect the energetic solar wind protons. Only the presence of electric fields, generated through ambipolar, Hall, or convective terms [see also, e.g., *Jarvinen et al.*, 2014; *Fatemi et al.*, 2014], were able to sufficiently reflect and or deflect the solar wind. Furthermore, the qualitative proton scattering function found by *Zimmerman et al.* [2015] as a function of solar zenith angle closely matches that found with ARTEMIS here, namely, isotropic scattering at low solar zenith angles and strong forward scattering at high solar zenith angles [i.e., *Zimmerman et al.*, 2015, Figure 6]. Furthermore, we note that analyses of Chandrayaan observations of reflected solar wind protons and a comparison of these observations to hybrid modeling found that a forward scattering function for protons off of crustal magnetic anomalies yielded the best fit to the data [*Lue et al.*, 2011; *Fatemi*, 2014]. The forward scattering of solar wind protons off of lunar magnetic anomalies is also distinctly different from solar wind proton scattering from the unmagnetized lunar surface, which has been observed as dominantly backscattered in both charged [*Saito et al.*, 2008; *Lue et al.*, 2016] and neutral forms [*Schaufelberger et al.*, 2011].

An accurate understanding of the proton reflection magnitude and scattering function has important implications in the study of the lunar plasma environment and lunar geophysics. As solar wind protons and alphas (He^{++}) impact the Moon, they induce optical and chemical changes in the lunar surface at a rate proportional to the incoming proton flux. A prominent chemical consequence of solar wind irradiation of the lunar surface is the production of OH and/or H_2O in lunar soil, which has been remotely observed at the Moon [e.g., *Pieters et al.*, 2009; *McCord et al.*, 2011; *Hendrix et al.*, 2012] and verified experimentally in laboratory settings [e.g., *Hibbits et al.*, 2011; *Burke et al.*, 2011; *Managadze et al.*, 2011; *Ichimura et al.*, 2012; *Poston et al.*, 2013; *Bradley et al.*, 2014]. Solar wind irradiation (along with micrometeoroid bombardment) also changes the albedo and spectra of lunar regolith via the production of nanophase iron embedded within the rims of lunar regolith grains (i.e. , "space weathering") [e.g., *Wiesli et al.*, 2003; *Noble et al.*, 2007; *Loeffler et al.*, 2009; *Hemingway et al.*, 2015]. Critically, *Hemingway et al.* [2015] have presented observations that show a latitudinal trend in space weathering signatures that matches weathering trends observed in lunar swirls, with higher rates of weathering found near the equatorial regions. This correlation supports the conclusion that solar wind irradiation of lunar material is a prominent process in the alteration of regolith optical properties and that variations in incident solar wind flux, including that induced by the shielding presence of crustal magnetic anomalies, may significantly alter the space weathering rates of the underlying regolith.

Variations in solar wind flux to the lunar surface also impact the lunar neutral exosphere and energetic neutral atom population via local suppression of proton implantation and/or reflection at the surface, which serves as a source of both ENAs [e.g., *Wieser et al.*, 2009; *Saul et al.*, 2013; *Allegrini et al.*, 2013] and exospheric H and H_2 [*Hodges*, 2011; *Stern et al.*, 2013; *Farrell et al.*, 2015; *Hurley et al.*, 2017], and suppression of local charged-particle sputtering, which serves as a source for various refractory species in the exosphere [*Wurz et al.*, 2007; *Sarantos et al.*, 2012]. Magnetic anomalies have been shown to locally suppress the flux of backscattered ENAs from the lunar surface as solar wind protons are reflected from electrostatic fields in charged form before striking the surface [*Wieser et al.*, 2010; *Vorburger et al.*, 2012; *Futaana et al.*, 2013]. For the sputtered lunar neutral exosphere, *Poppe et al.* [2014] made theoretical predictions for the degree to which exospheric neutral densities may be affected by the presence of crustal magnetic anomalies, finding that densities can be diminished by over an order of magnitude in crustal magnetic anomaly regions. Preliminary evidence for such an effect has been found in analysis of exospheric pickup ion distributions observed by the ARTEMIS mission [*Halekas et al.*, 2016]. Thus, the solar wind proton reflection percentage map constructed here is critical in correlating reduced solar wind sputtering fluxes with variations in both the fluxes of energetic neutral atoms and exospheric pickup ions.

Finally, the reflection and scattering function of solar wind protons from crustal magnetic anomalies has direct implications on the lunar near-space plasma environment. As protons reflected from crustal magnetic

anomalies gyrate around the interplanetary magnetic field, they can generate electromagnetic waves [e.g., *Halekas et al.*, 2006b, 2008, 2012; *Tsugawa et al.*, 2011; *Harada et al.*, 2015] and small-scale shocks in the solar wind [*Russell and Lichtenstein*, 1975; *Fatemi et al.*, 2014; *Halekas et al.*, 2014], and can gyrate into the low-density lunar wake, significantly disturbing the current and field structure behind the Moon [*Nishino et al.*, 2009, 2013; *Dhanya et al.*, 2016]. Understanding each of these phenomena requires knowledge of the scattered/reflected proton population from the Moon (including from both the unmagnetized and magnetized lunar surface); thus, the maps and scattering functions constructed here can be used in further modeling and data analysis studies.

6. Conclusion

We have compiled over 5 years of ARTEMIS observations of solar wind protons reflected from the lunar surface and crustal magnetic anomalies in order to construct a global proton reflection map and study the scattering characteristics of lunar crustal magnetic anomalies. For each ARTEMIS passage through a 2 R_L hemispherical volume on the dayside of the Moon, we used a Runge-Kutta algorithm to trace proton trajectories backward in time under the influence of the local electromagnetic fields. Liouville's Theorem provides that the proton distribution function is conserved along these trajectories and thus, the distribution function observed by ARTEMIS at each time, velocity, and angle can be associated with a corresponding reflected velocity and pair of scattering angles. By averaging together approximately 1.5×10^9 individual measurements of the reflected proton distribution function across the lunar surface and filling points in each local scattered distribution function not measured by ARTEMIS, we have constructed both a global map of proton reflection from the Moon as well as the angular scattering function of solar wind protons from the South Pole/Aitken Basin anomaly region.

The database of reflected proton observations constructed here should yield additional insight into the fundamental electromagnetic interactions of lunar crustal magnetic anomalies with the solar wind. Indeed, the observations of reflected solar wind fractions and scattering functions are critically important for comparison to the various hybrid and particle-in-cell simulations recently undertaken in an effort to understand the mechanism(s) underlying the interaction between lunar crustal anomalies and the solar wind. These (and other) simulations have suggested that solar wind reflection is sensitive to both the overall field strength and the topology of any given magnetic anomaly [*Deca et al.*, 2015; *Bamford et al.*, 2016; *Poppe et al.*, 2016]. One would also expect the response of lunar crustal magnetic anomalies to depend on the upstream parameters, including the solar wind density, velocity, and pressure [e.g., see *Fatemi et al.*, 2015], as well as the interplanetary magnetic field strength and direction. A combination of continued analysis of the ARTEMIS-reflected proton data set and comparison to high-quality modeling of lunar magnetic anomalies will provide continued insight into these unique examples of planetary magnetism.

Acknowledgments
The authors gratefully acknowledge support from NASA's Lunar Data Analysis Program, grant NNX15AP89G. The ARTEMIS mission is funded and operated under NASA grant NAS5-02099, and we specifically acknowledge J.P. McFadden for the use of ESA data and K.-H. Glassmeier, U. Auster, and W. Baumjohann for the use of FGM data provided under the lead of the Technical University of Braunschweig and with financial support through the German Ministry for Economy and Technology and the German Center for Aviation and Space (DLR), contract 50 OC 0302. All ARTEMIS data necessary to reproduce this work are publicly available at http://artemis.ssl.berkeley.edu.

References

Allegrini, F., et al. (2013), Lunar energetic neutral atom (ENA) spectra measured by the interstellar boundary explorer (IBEX), *Planet. Space Sci.*, *85*, 232–242.

Angelopoulos, V. (2011), The ARTEMIS mission, *Space Sci. Rev.*, *165*, 3–25.

Auster, H. U., et al. (2008), The THEMIS fluxgate magnetometer, *Space Sci. Rev.*, *141*, 235–264.

Bamford, R. A., et al. (2016), 3D PIC simulations of collisionless shocks at lunar magnetic anomalies and their role in forming lunar swirls, *Astrophys. J.*, *830*, 146.

Bradley, J. P., H. A. Ishii, J. J. Gillis-Davis, J. Ciston, M. H. Nielsen, H. A. Bechtel, and M. C. Martin (2014), Detection of solar wind-produced water in irradiated rims on silicate minerals, *Proc. Natl. Acad. Sci. U.S.A.*, *111*(5), 1732–1735.

Burke, D. J., C. A. Dukes, J.-H. Kim, J. Shi, M. Famá, and R. A. Baragiola (2011), Solar wind contribution to surficial lunar water: Laboratory investigations, *Icarus*, *211*, 1082–1088.

Deca, J., A. Divin, G. Lapenta, B. Lembège, S. Markidis, and M. Horányi (2014), Electromagnetic particle-in-cell simulations of the solar wind interaction with lunar magnetic anomalies, *Phys. Rev. Lett.*, *112*, 151102.

Deca, J., A. Divin, B. Lembège, M. Horányi, S. Markidis, and G. Lapenta (2015), General mechanism and dynamics of the solar wind interaction with lunar magnetic anomalies from 3-D particle-in-cell simulations, *J. Geophys. Res. Space Physics*, *120*, 6443–6463, doi:10.1002/2015JA021070.

Dhanya, M. B., A. Bhardwaj, Y. Futaana, S. Barabash, A. Alok, M. Wieser, M. Holmström, and P. Wurz (2016), Characteristics of proton velocity distribution functions in the near-lunar wake from Chandrayaan-1/SWIM observations, *Icarus*, *271*, 120–130.

Dmitriev, A. V., A. V. Suvorova, and I. S. Veselovsky (2011), Statistical characteristics of the heliospheric plasma and magnetic field at Earth's orbit during four solar cycles 20–23, in *Handbook on Solar Wind: Effects, Dynamics, and Interactions*, chap. 2, edited by H. E. Johannson, pp. 81–144, NOVA Science Publishers, New York.

Farrell, W. M., D. M. Hurley, and M. I. Zimmerman (2015), Solar wind implantation into lunar regolith: Hydrogen retention in a surface with defects, *Icarus*, *255*, 116–126.

Fatemi, S. (2014), Kinetic modeling of the solar wind plasma interaction with the Moon, PhD thesis, Swedish Institute of Space Physics, LuleåUniv. of Technology, Luleå, Sweden.

Fatemi, S., M. Holmström, and Y. Futaana (2012), The effects of lunar surface plasma absorption and solar wind temperature anisotropies on the solar wind proton velocity space distributions in the low-altitude lunar plasma wake, *J. Geophys. Res.*, *117*, A10105, doi:10.1029/2011JA017353.

Fatemi, S., M. Holmström, Y. Futaana, C. Lue, M. R. Collier, S. Barabash, and G. Stenberg (2014), Effects of protons reflected by lunar crustal magnetic fields on the global lunar plasma environment, *J. Geophys. Res. Space Physics*, *119*, 6095–6105, doi:10.1002/2014JA019900.

Fatemi, S., C. Lue, M. Holmström, A. R. Poppe, M. Wieser, S. Barabash, and G. T. Delory (2015), Solar wind plasma interaction with Gerasimovich lunar magnetic anomaly, *J. Geophys. Res. Space Physics*, *120*, 4719–4735, doi:10.1002/2015JA021027.

Futaana, Y., S. Machida, Y. Saito, A. Matsuoka, and H. Hayakama (2003), Moon-related nonthermal ions observed by Nozomi: Species, sources, and generation mechanisms, *J. Geophys. Res.*, *108*(A1), 1025, doi:10.1029/2002JA009366.

Futaana, Y., S. Barabash, M. Wieser, C. Lue, P. Wurz, A. Vorburger, A. Bhardwaj, and K. Asamura (2013), Remote energetic neutral atom imaging of electric potential over a lunar magnetic anomaly, *Geophys. Res. Lett.*, *40*, 262–266, doi:10.1002/grl.50135.

Giacalone, J., and L. L. Hood (2015), Hybrid simulation of the interaction of solar wind protons with a concentrated lunar magnetic anomaly, *J. Geophys. Res. Space Physics*, *120*, 4081–4094, doi:10.1002/2014JA020938.

Halekas, J. S., D. L. Mitchell, R. P. Lin, S. Frey, L. L. Hood, M. H. Acuña, and A. B. Binder (2001), Mapping of crustal magnetic anomalies on the lunar near side by the Lunar Prospector electron reflectometer, *J. Geophys. Res.*, *106*(E11), 27,841–27,852.

Halekas, J. S., D. A. Brain, D. L. Mitchell, R. P. Lin, and L. Harrison (2006a), On the occurrence of magnetic enhancements caused by solar wind interaction with lunar crustal fields, *Geophys. Res. Lett.*, *33*, L08106, doi:10.1029/2006GL025931.

Halekas, J. S., D. A. Brain, D. L. Mitchell, and R. P. Lin (2006b), Whistler waves observed near lunar crustal magnetic sources, *Geophys. Res. Lett.*, *33*, L22104, doi:10.1029/2006GL027684.

Halekas, J. S., D. A. Brain, R. P. Lin, and D. L. Mitchell (2008), Solar wind interaction with lunar crustal magnetic anomalies, *Adv. Space Res.*, *41*, 1319–1324.

Halekas, J. S., A. R. Poppe, W. M. Farrell, G. T. Delory, V. Angelopoulos, J. P. McFadden, J. W. Bonnell, K. H. Glassmeier, F. Plaschke, A. Roux, O. LeContel, and R. E. Ergun (2012), Lunar precursor effects in the solar wind and terrestrial magnetosphere, *J. Geophys. Res.*, *117*, A05101, doi:10.1029/2011JA017289.

Halekas, J. S., A. R. Poppe, J. P. McFadden, and K.-H. Glassmeier (2013), The effects of reflected protons on the plasma environment of the Moon for parallel interplanetary magnetic fields, *Geophys. Res. Lett.*, *40*, 4544–4548, doi:10.1002/grl.50892.

Halekas, J. S., A. R. Poppe, J. P. McFadden, V. Angelopoulos, K.-H. Glassmeier, and D. A. Brain (2014), Evidence for small-scale collisionless shocks at the Moon from ARTEMIS, *Geophys. Res. Lett.*, *41*, 7436–7443, doi:10.1002/2014GL061973.

Halekas, J. S., A. R. Poppe, W. M. Farrell, and J. P. McFadden (2016), Structure and composition of the distant lunar exosphere: Constraints from ARTEMIS observations of ion acceleration in time-varying fields, *J. Geophys. Res. Planets*, *121*, 1102–1115, doi:10.1002/2016JE005082.

Harada, Y., J. S. Halekas, A. R. Poppe, Y. Tsugawa, S. Kurita, and J. P. McFadden (2015), Statistical characterization of the foremoon particle and wave morphology: ARTEMIS observations, *J. Geophys. Res. Space Physics*, *120*, 4907–4921, doi:10.1002/2015JA021211.

Harnett, E. M., and R. M. Winglee (2002), 2.5D particle and MHD simulations of mini-magnetospheres at the Moon, *J. Geophys. Res.*, *107*(A12), 1421, doi:10.1029/2002JA009241.

Harnett, E. M., and R. M. Winglee (2003), 2.5-D simulations of the solar wind interacting with multiple dipoles on the surface of the Moon, *J. Geophys. Res.*, *108*(A2), 1088, doi:10.1029/2002JA009617.

Hemingway, D. J., I. Garrick-Bethell, and M. A. Kreslavsky (2015), Latitudinal variation in spectral properties of the lunar maria and implications for space weathering, *Icarus*, *261*, 66–79.

Hendrix, A. R., et al. (2012), The lunar far-UV albedo: Indicator of hydration and weathering, *J. Geophys. Res.*, *117*, E12001, doi:10.1029/2012JE004252.

Hibbits, C. A., G. A. Grieves, M. J. Poston, M. D. Dyar, A. B. Aleksandrov, M. A. Johnson, and T. M. Orlando (2011), Thermal stability of water and hydroxyl on the surface of the Moon from temperature-programmed desorption measurements of lunar analog materials, *Icarus*, *213*, 64–72.

Hodges, R. R. (2011), Resolution of the lunar hydrogen enigma, *Geophys. Res. Lett.*, *38*, L06201, doi:10.1029/2012JE004252.

Hood, L. L., and G. Schubert (1980), Lunar magnetic anomalies and surface optical properties, *Science*, *208*, 49–51.

Hood, L. L., and C. R. Williams (1989), The lunar swirls: Distribution and possible origins, in *Proceedings of 19th Lunar Science Conference*, vol. 19, pp. 99–113, Cambridge Univ. Press, Cambridge, U. K.

Hood, L. L., C. T. Russell, and P. J. Coleman Jr. (1981), Contour maps of lunar remanent magnetic fields, *J. Geophys. Res.*, *86*(B2), 1055–1069.

Hurley, D. M., et al. (2017), Contributions of solar wind and micrometeoroids to molecular hydrogen in the lunar exosphere, *Icarus*, *283*, 31–37.

Ichimura, A. S., A. P. Zent, R. C. Quinn, M. R. Sanchez, and L. A. Taylor (2012), Hydroxyl (OH) production on airless planetary bodies: Evidence from H^+/D^+ ion-beam experiments, *Earth Plan. Sci. Lett.*, *345-348*, 90–94.

Jarvinen, R., M. Alho, E. Kallio, P. Wurz, S. Barabash, and Y. Futaana (2014), On vertical electric fields at lunar magnetic anomalies, *Geophys. Res. Lett.*, *41*, 2243–2249, doi:10.1002/2014GL059788.

Kramer, G. Y., et al. (2011), M^3 spectral analysis of lunar swirls and the link between optical maturation and surface hydroxyl formation at magnetic anomalies, *J. Geophys. Res.*, *116*, E00G18, doi:10.1029/2010JE00.

Loeffler, M. J., C. A. Dukes, and R. A. Baragiola (2009), Irradiation of olivine by 4 keV He^+: Simulation of space weathering by the solar wind, *J. Geophys. Res.*, *114*, E03003, doi:10.1029/2008JE003249.

Lue, C., Y. Futaana, S. Barabash, M. Wieser, M. Holmström, A. Bhardwaj, M. B. Dhanya, and P. Wurz (2011), Strong influence of lunar crustal fields on the solar wind flow, *Geophys. Res. Lett.*, *38*, L03202, doi:10.1029/2010GL046215.

Lue, M. C., J. S. Halekas, A. R. Poppe, and J. P. McFadden (2016), ARTEMIS observations of proton scattering off the lunar surface, Abstract 2230 presented at 2016 Fall Meeting, AGU, San Francisco, Calif., 2016 Dec.

Managadze, G. G., V. T. Cherepin, Y. G. Shkuratov, V. N. Kolesnik, and A. E. Chumikov (2011), Simulating OH/H_2O formation by solar wind at the lunar surface, *Icarus*, *215*, 449–451.

McCord, T. B., L. A. Taylor, J.-P. Combe, G. Kramer, C. M. Pieters, J. M. Sunshine, and R. N. Clark (2011), Sources and physical processes responsible for OH/H_2O in the lunar soil as revealed by the Moon Mineralogy Mapper (M^3), *J. Geophys. Res.*, *116*, E00G05, doi:10.1029/2010JE003711.

McFadden, J. P., et al. (2008), The THEMIS ESA plasma instrument and in-flight calibration, *Space Sci. Rev.*, *141*, 277–302.

Mitchell, D. L., J. S. Halekas, R. P. Lin, S. Frey, L. L. Hood, M. H. Acuña, and A. Binder (2008), Global mapping of lunar crustal magnetic fields by Lunar Prospector, *Icarus*, *194*, 401–409.

Nishino, M. N., et al. (2009), Solar-wind proton access deep into the near-Moon wake, *Geophys. Res. Lett.*, *36*, L16103, doi:10.1029/2009GL039444.
Nishino, M. N., et al. (2013), Type-II entry of solar wind protons into the lunar wake: Effects of magnetic connection to the night-side surface, *Planet. Space Sci.*, *87*, 106–114.
Noble, S. K., C. M. Pieters, and L. P. Keller (2007), An experimental approach to understanding the optical effects of space weathering, *Icarus*, *192*, 629–642.
Pieters, C. M., et al. (2009), Character and spatial distribution of OH/H_2O on the surface of the Moon seen by M^3 on Chandrayaan-1, *Science*, *326*, 568–572.
Poppe, A. R., J. S. Halekas, G. T. Delory, and W. M. Farrell (2012), Particle-in-cell simulations of the solar wind interactions with lunar crustal magnetic anomalies: Magnetic cusp regions, *J. Geophys. Res.*, *117*, A09105, doi:10.1029/2012JA017844.
Poppe, A. R., M. Sarantos, J. S. Halekas, G. T. Delory, Y. Saito, and M. Nishino (2014), Anisotropic solar wind sputtering of the lunar surface induced by crustal magnetic anomalies, *Geophys. Res. Lett.*, *41*, 4865–4872, doi:10.1002/2014GL060523.
Poppe, A. R., S. Fatemi, I. Garrick-Bethell, D. Hemingway, and M. Holmström (2016), Solar wind interaction with the Reiner Gamma crustal magnetic anomaly: Connecting source magnetization to surface weathering, *Icarus*, *266*, 261–266.
Poston, M. J., G. A. Grieves, A. B. Aleksandrov, C. A. Hibbits, M. D. Dyar, and T. M. Orlando (2013), Water interactions with micronized lunar surrogates JSC-1A and albite under ultra-high vacuum with application to lunar observations, *J. Geophys. Res. Planets*, *118*, 105–115, doi:10.1029/2012JE004283.
Purucker, M. E., and J. B. Nicholas (2010), Global spherical harmonic models of the internal magnetic field of the Moon based on sequential and coestimation approaches, *J. Geophys. Res.*, *115*, E12007, doi:10.1029/2010JE003650.
Richmond, N. C., L. L. Hood, J. S. Halekas, D. L. Mitchell, R. P. Lin, M. Acuña, and A. B. Binder (2003), Correlation of a strong lunar magnetic anomaly with a high-albedo region of the Descartes mountains, *Geophys. Res. Lett.*, *30*(7), 1395, doi:10.1029/2003GL016938.
Russell, C. T., and B. R. Lichtenstein (1975), On the source of lunar limb compressions, *J. Geophys. Res.*, *80*(34), 4700–4711.
Russell, C. T., P. J. Coleman Jr., B. R. Lichtenstein, G. Schubert, and L. R. Sharp (1973), Subsatellite measurements of the lunar magnetic field, in *Proceedings of 4th Lunar Science Conference*, vol. 3, pp. 2833–2845, Houston, Tex.
Saito, Y., M. N. Nishino, M. Fujimoto, T. Yamamoto, S. Yokota, H. Tsunakawa, H. Shibuya, M. Matsushima, H. Shimizu, and F. Takahashi (2012), Simultaneous observation of the electron acceleration and ion deceleration over lunar magnetic anomalies, *Earth Planets Space*, *64*, 83–92.
Saito, Y., et al. (2008), Solar wind proton reflection at the lunar surface: Low energy ion measurement by MAP-PACE onboard SELENE (KAGUYA), *Geophys. Res. Lett.*, *35*, L24205, doi:10.1029/2008GL036077.
Saito, Y., et al. (2010), In-flight performance and initial results of plasma energy angle and composition Experiment (PACE) on SELENE (Kaguya), *Space Sci. Rev.*, *154*, 265–303.
Sarantos, M., R. M. Killen, D. A. Glenar, M. Benna, and T. J. Stubbs (2012), Metallic species, oxygen and silicon in the lunar exosphere: Upper limits and prospects for LADEE measurements, *J. Geophys. Res.*, *117*, A03103, doi:10.1029/2011JA017044.
Saul, L., P. Wurz, A. Vorburger, D. F. Rodríguez, S. A. Fuselier, D. J. McComas, E. Möbius, S. Barabash, H. Funsten, and P. Janzen (2013), Solar wind reflection from the lunar surface: The view from far and near, *Planet. Space Sci.*, *84*, 1–4.
Schaufelberger, A., P. Wurz, S. Barabash, M. Wieser, Y. Futaana, M. Holmström, A. Bhardwaj, M. B. Dhanya, R. Sridharan, and K. Asamura (2011), Scattering function for energetic neutral hydrogen atoms off the lunar surface, *Geophys. Res. Lett.*, *38*, L22202, doi:10.1029/2011GL049362.
Stern, S. A., J. C. Cook, J.-Y. Chaufray, P. D. Feldman, G. R. Gladstone, and K. D. Retherford (2013), Lunar atmospheric H_2 detections by the LAMP UV spectrograph on the Lunar Reconnaissance Orbiter, *Icarus*, *226*, 1210–1213.
Sweetser, T. H., S. B. Brochart, V. Angelopoulos, G. J. Whiffen, D. C. Folta, M.-K. Chung, S. J. Hatch, and M. A. Woodard (2011), ARTEMIS mission design, *Space Sci. Rev.*, *165*(1-4), 27–57.
Tsugawa, Y., N. Terada, Y. Katoh, T. Ono, H. Tsunakawa, F. Takahashi, H. Shibuya, H. Shimizu, and M. Matsushima (2011), Statistical analysis of monochromatic whistler waves near the Moon detected by Kaguya, *Ann. Geophys.*, *29*, 889–893.
Vorburger, A., P. Wurz, S. Barabash, M. Wieser, Y. Futaana, M. Holmström, A. Bhardwaj, and K. Asamura (2012), Energetic neutral atom observations of magnetic anomalies on the lunar surface, *J. Geophys. Res.*, *117*, A07208, doi:10.1029/2012JA017553.
Wang, X., M. Horányi, and S. Robertson (2012), Characteristics of a plasma sheath in a magnetic dipole field: Implications to the solar wind interaction with the lunar magnetic anomalies, *J. Geophys. Res.*, *117*, A06226, doi:10.1029/2012JA017635.
Wang, X., C. T. Howes, M. Horányi, and S. Robertson (2013), Electric potentials in magnetic dipole fields normal and oblique to a surface in plasma: Understanding the solar wind interaction with lunar magnetic anomalies, *Geophys. Res. Lett.*, *40*, 1686–1690, doi:10.1002/grl.50367.
Wieser, M., S. Barabash, Y. Futaana, M. Holmström, A. Bhardwaj, R. Sridharan, M. B. Dhanya, P. Wurz, A. Schaufelberger, and K. Asamura (2009), Extremely high reflection of solar wind protons as neutral hydrogen atoms from regolith in space, *Planet. Space Sci.*, *57*, 2132–2134.
Wieser, M., S. Barabash, Y. Futaana, M. Holmström, A. Bhardwaj, R. Sridharan, M. B. Dhanya, A. Schaufelberger, P. Wurz, and K. Asamura (2010), First observation of a mini-magnetosphere above a lunar magnetic anomaly using energetic neutral atoms, *Geophys. Res. Lett.*, *37*, L05103, doi:10.1029/2009GL041721.
Wiesli, R. A., B. L. Beard, L. A. Taylor, and C. M. Johnson (2003), Space weathering processes on airless bodies: Fe isotope fractionation in the lunar regolith, *Earth Planet. Sci. Lett.*, *216*, 457–465.
Wurz, P., U. Rohner, J. A. Whitby, C. Kolb, H. Lammer, P. Dobnikar, and J. A. Martín-Fernández (2007), The lunar exosphere: The sputtering contribution, *Icarus*, *191*, 486–496.
Xie, L., L. Li, Y. Zhang, Y. Feng, X. Wang, A. Zhang, and L. Kong (2015), Three-dimensional Hall MHD simulation of lunar minimagnetosphere: General characteristics and comparison with Chang'E-2 observations, *J. Geophys. Res. Space Physics*, *120*, 6559–6568, doi:10.1002/2015JA021647.
Zimmerman, M. I., W. M. Farrell, and A. R. Poppe (2015), Kinetic simulations of kilometer-scale mini-magnetosphere formation on the Moon, *J. Geophys. Res. Planets*, *120*, 1893–1903, doi:10.1002/2015JE004865.